REVISTA
INTERDISCIPLINAR DE
PESQUISA EM
ENGENHARIA

CILAMCE
2016

XXXVII IBERIAN LATIN AMERICAN CONGRESS
ON COMPUTATIONAL METHODS IN ENGINEERING
BRASÍLIA - DF - BRAZIL

FLOW OF AN EMULSION DROP THROUGH A CONVERGING CHANNEL USING THE BOUNDARY ELEMENT METHOD

Lucas Hildebrand Pires da Cunha

Éder Lima de Albuquerque

lucashilde@gmail.com

eder@unb.br

Department of Mechanical Engineering, Universidade de Brasília

Campus Universitário Darcy Ribeiro, 70910-900, DF, Brasília, Brazil

Ivan Rosa de Siqueira

ivan@lmmp.mec.puc-rio.br

Laboratory of Microhydrodynamics and Flow in Porous Media - LMMP, Department of Mechanical Engineering, Pontifícia Universidade Católica do Rio de Janeiro

R. Marquês de São Vincente - 225 Gávea, 22451-900, RJ, Rio de Janeiro, Brazil

Abstract. *The Boundary Element Method is employed to simulate the flow of a planar emulsion drop through a converging channel. The physical flow parameters allow to describe it using Stokes equations. A verification on the method accuracy and convergence is done related to the mesh and time increment refinement. The pump pressure answer, during the drop flow to keep the flow rate, is studied in relation to the capillary number, the viscosity ratio and the drop initial diameter.*

Keywords: *Emulsion, Planar drop, Porous media, Boundary Element Method.*

1 INTRODUCTION

The use of oil-water emulsions as a mobility control agent in enhanced oil recovery processes in order to achieve a more efficient sweep of the petroleum reservoir is a widespread theme in the current literature (Alvarado & Manrique, 2010). The macroscopic behavior of these methods is intrinsically related to the pore-scale flow. Since the drop diameter has the same order of magnitude of the pore throats dimensions, the emulsion cannot be treated as a singe phase non-Newtonian fluid. Otherwise, this complex liquid must be modeled as a biphasic mixture of two immiscible viscous Newtonian fluids. Several experimental results and theoretical analysis have shown that for the emulsion flow, the pressure drop at a fixed flow rate is raised by two distinct mechanisms: a viscous effect related to the presence of the high viscosity oil phase and a capillary effect related to the deformation of the droplet interface as it flows through the porous throat (Roca & Carvalho, 2013). Within this context, the present work aims to perform a numerical investigation of the flow of an emulsion drop though a porous media using the Boundary Element Method (BEM).

The model considers the flow of a single planar oil droplet through a converging channel representing the porous throat, and can provide important qualitative results in this type of study. The flow is free from inertial effects and thereby it is governed by the Stokes' incompressible equations. In this sense, a boundary integral formulation based on line integrals over the drop surface and the channel boundaries relating both velocity and stress fields can be obtained. Several numerical aspects of the method are discussed in details, including the use of quadratic continuous boundary elements, the interpolation of the unknown fields using second-order shape function and, the discretization and numerical solution of the integral equations. The results show the effects of physical and geometric parameters, such as the fluids viscosity ratio, capillary number and droplet initial diameter on the flow rate-pressure drop relation and on the droplet shape in the flow.

2 MATHEMATICAL MODELING

A scheme of the problem is represented in Fig. 1. Both phases are composed by incompressible Newtonian liquids with the same density ρ. The drop is initially spherical with diameter a and viscosity $\lambda\mu$, and it is immersed in other fluid with the viscosity equal to μ. Here, H and h are the height of the entrance and exit (throat) of the channel, and P_0 and P_L are the inlet and outlet pressure, respectively. Each fluid occupies a region Ω limited by a contour Γ, and the subscripts i and o are used to correspond to the inner and outer fluids, respectively.

Due the physical parameters associated to the inner and outer flows, the inertial forces are neglectable comparing to viscous ones ($Re \ll 1$).

2.1 Stokes flow integral representation

According to Kim & Karrila (1991), the flow of a Newtonian incompressible fluid free from inertial effects is governed by the Stokes' equations shown in Eq. (1) and Eq. (2), where $\boldsymbol{\sigma}$ is the stress tensor field and $\boldsymbol{u}$ is the velocity field, respectively.

$$\nabla \cdot \boldsymbol{u} = 0. \tag{1}$$

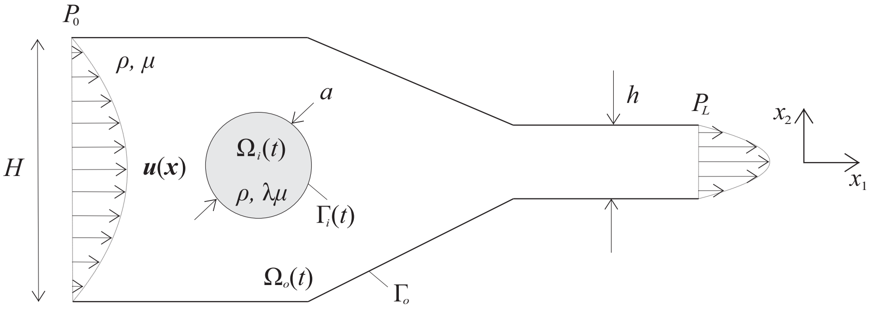

Figure 1: Scheme of the planar drop dispersed in other immiscible fluid flowing through a converging channel. The drop is composed by the *i* fluid while the continuous one is compose by the *o* fluid. Each fluid occupies a region Ω limited by a contour Γ.

$$\nabla \cdot \boldsymbol{\sigma} = \mathbf{0}. \tag{2}$$

The stress tensor, $\boldsymbol{\sigma}$, is given by,

$$\boldsymbol{\sigma}(\boldsymbol{x}) = -p(\boldsymbol{x})\boldsymbol{I} + 2\mu\boldsymbol{D}, \tag{3}$$

where $\boldsymbol{I}$ is the unit tensor, $p(\boldsymbol{x})$ is the mechanical pressure and $\boldsymbol{D} = \frac{1}{2}(\nabla\boldsymbol{u} + \nabla\boldsymbol{u}^T)$.

The Stokes flow integral representation in a domain Ω limited by a contour Γ can be obtained utilizing the fundamental solution of Stokes flow created by a force point in an infinite fluid domain, presented by Ladyzheskaya (1969), and the Lorentz Reciprocity Theorem (Kim & Karrila, 1991; Pozrikids, 1992). After all, the velocity on a point $\boldsymbol{x}_0$ can be obtained using,

$$\left.\begin{array}{ll} \boldsymbol{x}_0 \in \Omega, & \boldsymbol{u}(\boldsymbol{x}_0) \\ \boldsymbol{x}_0 \in \Gamma, & c(\boldsymbol{x}_0)\boldsymbol{u}(\boldsymbol{x}_0) \\ \boldsymbol{x}_0 \notin \Omega, & \mathbf{0} \end{array}\right\} = \frac{1}{4\pi\mu}\int_\Gamma \boldsymbol{\mathcal{J}}(\boldsymbol{x}-\boldsymbol{x}_0)\cdot\boldsymbol{\sigma}(\boldsymbol{x})\cdot\hat{\boldsymbol{n}}\,d\Gamma(\boldsymbol{x}) - \frac{1}{4\pi}\int_\Gamma \boldsymbol{u}(\boldsymbol{x})\cdot\boldsymbol{\mathcal{K}}(\boldsymbol{x}-\boldsymbol{x}_0)\cdot\hat{\boldsymbol{n}}\,d\Gamma(\boldsymbol{x}), \tag{4}$$

where $c(\boldsymbol{x}_0)$ is a constant resultant from the Dirac Delta function integration and depend on the contour geometry, $\hat{\boldsymbol{n}}$ is the contour normal direction and, $\boldsymbol{\mathcal{J}}$ and $\boldsymbol{\mathcal{K}}$ are both Green functions, given by

$$\boldsymbol{\mathcal{J}}(\boldsymbol{x}-\boldsymbol{x}_0) = \boldsymbol{I}\log\left(\frac{1}{|\boldsymbol{x}-\boldsymbol{x}_0|}\right) + \frac{(\boldsymbol{x}-\boldsymbol{x}_0)(\boldsymbol{x}-\boldsymbol{x}_0)}{|\boldsymbol{x}-\boldsymbol{x}_0|^2}, \tag{5}$$

and

$$\boldsymbol{\mathcal{K}}(\boldsymbol{x}-\boldsymbol{x}_0) = -4\frac{(\boldsymbol{x}-\boldsymbol{x}_0)(\boldsymbol{x}-\boldsymbol{x}_0)(\boldsymbol{x}-\boldsymbol{x}_0)}{|\boldsymbol{x}-\boldsymbol{x}_0|^4}. \tag{6}$$

2.2 Flow integral representation on the interface

The relation between the inner and outer flows are obtained using the boundary conditions on the interface. Due the continuity in velocity, the two flows should have the same velocity over the shared points, such that

$$\boldsymbol{u}_i(\boldsymbol{x}) = \boldsymbol{u}_o(\boldsymbol{x})\,, \;\; \boldsymbol{x} \in \Gamma_i(t). \tag{7}$$

There is no continuity in the stress tensor on the interface, but it is possible to calculate the stress jump over the normal direction, $\Delta\boldsymbol{f}(\boldsymbol{x},t) = [\boldsymbol{\sigma}_o(\boldsymbol{x},t) - \boldsymbol{\sigma}_i(\boldsymbol{x},t)] \cdot \hat{\boldsymbol{n}}(\boldsymbol{x},t)$, using the Young-Laplace equation,

$$\Delta\boldsymbol{f}(\boldsymbol{x},t) = \sigma\kappa(\boldsymbol{x},t)\hat{\boldsymbol{n}}(\boldsymbol{x},t)\,, \;\; \boldsymbol{x} \in \Gamma_i(t), \tag{8}$$

where, σ is the interfacial tension between the fluids and κ is the surface curvature.

Using the velocity and tension relations over the fluids interface, it is possible to calculate the velocity over Γ_i and Γ_o by the dimensionless[1] Eqs. (9) and (10), respectively.

$$\begin{aligned}
\boldsymbol{x}_0 \in \Gamma_i(t),\; c(\boldsymbol{x}_0,t)(\lambda+1)\boldsymbol{u}_i(\boldsymbol{x}_0,t) &= \frac{1}{4\pi}\int_{\Gamma_o} \boldsymbol{\mathcal{J}}(\boldsymbol{x}-\boldsymbol{x}_0)\cdot\boldsymbol{t}_o(\boldsymbol{x},t)\,d\Gamma \\
&- \frac{1}{4\pi}\int_{\Gamma_o} \boldsymbol{u}_o(\boldsymbol{x},t)\cdot\boldsymbol{\mathcal{K}}(\boldsymbol{x}-\boldsymbol{x}_0)\cdot\hat{\boldsymbol{n}}(\boldsymbol{x},t)\,d\Gamma \\
&+ \frac{1}{4\pi}Ca^{-1}\int_{\Gamma_i(t)} \boldsymbol{\mathcal{J}}(\boldsymbol{x}-\boldsymbol{x}_0)\cdot\kappa(\boldsymbol{x},t)\hat{\boldsymbol{n}}(\boldsymbol{x},t)\,d\Gamma \\
&- \frac{1-\lambda}{4\pi}\left(\frac{a}{H}\right)\int_{\Gamma_i(t)} \boldsymbol{u}_i(\boldsymbol{x},t)\cdot\boldsymbol{\mathcal{K}}(\boldsymbol{x}-\boldsymbol{x}_0)\cdot\hat{\boldsymbol{n}}(\boldsymbol{x},t)\,d\Gamma.
\end{aligned} \tag{9}$$

$$\begin{aligned}
\boldsymbol{x}_0 \in \Gamma_o,\; c(\boldsymbol{x}_0,t)\boldsymbol{u}_o(\boldsymbol{x}_0,t) &= \frac{1}{4\pi}\int_{\Gamma_o} \boldsymbol{\mathcal{J}}(\boldsymbol{x}-\boldsymbol{x}_0)\cdot\boldsymbol{t}_o(\boldsymbol{x},t)\,d\Gamma \\
&- \frac{1}{4\pi}\int_{\Gamma_o} \boldsymbol{u}_o(\boldsymbol{x},t)\cdot\boldsymbol{\mathcal{K}}(\boldsymbol{x}-\boldsymbol{x}_0)\cdot\hat{\boldsymbol{n}}(\boldsymbol{x},t)\,d\Gamma \\
&+ \frac{1}{4\pi}Ca^{-1}\int_{\Gamma_i(t)} \boldsymbol{\mathcal{J}}(\boldsymbol{x}-\boldsymbol{x}_0)\cdot\kappa(\boldsymbol{x},t)\hat{\boldsymbol{n}}(\boldsymbol{x},t)\,d\Gamma \\
&- \frac{1-\lambda}{4\pi}\left(\frac{a}{H}\right)\int_{\Gamma_i(t)} \boldsymbol{u}_i(\boldsymbol{x},t)\cdot\boldsymbol{\mathcal{K}}(\boldsymbol{x}-\boldsymbol{x}_0)\cdot\hat{\boldsymbol{n}}(\boldsymbol{x},t)\,d\Gamma.
\end{aligned} \tag{10}$$

The capillary number, Ca, present in Eqs. (9) and (10) is one of the most important parameters in emulsion rheology studies. It represents the relation between viscous forces and surface forces associated to interfacial tension, and it is given by $Ca = \mu U/\sigma$. Still in these equations, the normal vector over the channel contour points to the outside, while over the interface it points to the inside.

3 NUMERICAL METHODOLOGY

The solution of the problem is given by a boundary integral over the contour of the channel and over the drop interface. Therefore, we employed the BEM to numerically solve the problem.

---

[1] The dimensionless variables are defined as: $\boldsymbol{x}_0 = \boldsymbol{x}_0'/H$, $\boldsymbol{x} = \boldsymbol{x}'/H$, $\boldsymbol{u}_i = \boldsymbol{u}_i'/U$, $\boldsymbol{u}_o = \boldsymbol{u}_o'/U$, $\boldsymbol{t}_o = H\boldsymbol{t}_o'/\mu U$, $\kappa = a\kappa'$, $\boldsymbol{\mathcal{J}} = \boldsymbol{\mathcal{J}}'$, $\boldsymbol{\mathcal{K}} = H\boldsymbol{\mathcal{K}}'$, $d\Gamma = d\Gamma'/H$ over Γ_o and $d\Gamma = d\Gamma'/a$ over $\Gamma_i(t)$, where $'$ denotes the dimensional variable.

The contours were divided in $N_o + N_i$ elements, being N_o for the outer contour (Γ_o) and N_i for the inner one (Γ_i). It was chosen the continuous quadratic element. In this case, every element is composed by three nodes, sharing the two nodes on the extremes with the neighboring elements. The use of shape functions allows to interpolate any vector variable by its values on the nodes,

$$\boldsymbol{x} = \left\{ \begin{array}{c} x_1 \\ x_2 \end{array} \right\} = \left[\begin{array}{cccccc} N_1 & 0 & N_2 & 0 & N_3 & 0 \\ 0 & N_1 & 0 & N_2 & 0 & N_3 \end{array} \right] \left\{ \begin{array}{c} x_1^{(1)} \\ x_2^{(1)} \\ x_1^{(2)} \\ x_2^{(2)} \\ x_1^{(3)} \\ x_2^{(3)} \end{array} \right\} = \boldsymbol{N}(\xi) \cdot \boldsymbol{x}_{(n)}, \tag{11}$$

where $\boldsymbol{x}_d^{(n)}$ is the variable value on the node n and direction d, ξ is the local spatial coordinate of the element which goes form -1 to 1, and N_s is the value of the shape functions s for ξ,

$$N_1 = \frac{\xi}{2}(\xi - 1), \tag{12}$$

$$N_2 = (1 - \xi)(1 + \xi) \tag{13}$$

and

$$N_3 = \frac{\xi}{2}(\xi + 1). \tag{14}$$

The discretization of the contours in elements and use of quadratic shape functions allow to rewrite Eqs. (9) and (10), respectively, as

$$\begin{aligned} \boldsymbol{x}_m \in \Gamma_i(t), c^m(\lambda + 1)\boldsymbol{u}_i^m(t) \quad = \quad & \frac{1}{4\pi} \sum_{n=1}^{N_o} \left(\int_{\Delta\Gamma_o^n} \boldsymbol{\mathcal{J}}^{mn} \cdot \boldsymbol{N}(\xi)\, d\Gamma \right) \cdot \boldsymbol{t}_{o(n)}(t) \\ - \quad & \frac{1}{4\pi} \sum_{n=1}^{N_o} \left(\int_{\Delta\Gamma_o^n} \boldsymbol{\mathcal{K}}^{mn} \cdot \hat{\boldsymbol{n}}^n(\xi, t) \cdot \boldsymbol{N}(\xi)\, d\Gamma \right) \cdot \boldsymbol{u}_{o(n)}(t) \\ + \quad & \frac{1}{4\pi} Ca^{-1} \sum_{n=N_o+1}^{N_o+N_i} \left(\int_{\Delta\Gamma_i^n} \boldsymbol{\mathcal{J}}^{mn} \cdot \kappa^n(\xi, t) \hat{\boldsymbol{n}}^n(\xi, t)\, d\Gamma \right) \\ - \quad & \frac{1 - \lambda}{4\pi} \left(\frac{a}{H} \right) \sum_{n=N_o+1}^{N_o+N_i} \left(\int_{\Delta\Gamma_i^n} \boldsymbol{\mathcal{K}}^{mn} \cdot \hat{\boldsymbol{n}}^n(\xi, t) \cdot \boldsymbol{N}(\xi)\, d\Gamma \right) \cdot \boldsymbol{u}_{i(n)}(t), \end{aligned} \tag{15}$$

and

$$\begin{aligned}\boldsymbol{x}_m \in \Gamma_o, c^m \boldsymbol{u}_o^m(t) &= \frac{1}{4\pi}\sum_{n=1}^{N_o}\left(\int_{\Delta\Gamma_o^n}\boldsymbol{\mathcal{J}}^{mn}\cdot\boldsymbol{N}(\xi)\,d\Gamma\right)\cdot\boldsymbol{t}_{o(n)}(t)\\ &- \frac{1}{4\pi}\sum_{n=1}^{N_o}\left(\int_{\Delta\Gamma_o^n}\boldsymbol{\mathcal{K}}^{mn}\cdot\hat{\boldsymbol{n}}^n(\xi,t)\cdot\boldsymbol{N}(\xi)\,d\Gamma\right)\cdot\boldsymbol{u}_{o(n)}(t)\\ &+ \frac{1}{4\pi}Ca^{-1}\sum_{n=N_o+1}^{N_o+N_i}\left(\int_{\Delta\Gamma_i^n}\boldsymbol{\mathcal{J}}^{mn}\cdot\kappa^n(\xi,t)\hat{\boldsymbol{n}}^n(\xi,t)\,d\Gamma\right)\\ &- \frac{1-\lambda}{4\pi}\left(\frac{a}{H}\right)\sum_{n=N_o+1}^{N_o+N_i}\left(\int_{\Delta\Gamma_i^n}\boldsymbol{\mathcal{K}}^{mn}\cdot\hat{\boldsymbol{n}}^n(\xi,t)\cdot\boldsymbol{N}(\xi)\,d\Gamma\right)\cdot\boldsymbol{u}_{i(n)}(t).\end{aligned} \tag{16}$$

The subscripts m and n determine that the functions are evaluated on the points $\boldsymbol{x}_m$ and $\boldsymbol{x}_n$, respectively. Khayat et al. (1997) showed that it is possible to compact these two equations in a linear system like $\boldsymbol{H}\cdot\boldsymbol{U} = \boldsymbol{G}\cdot\boldsymbol{T}+\boldsymbol{B}$, where $\boldsymbol{H}$ and $\boldsymbol{G}$ are matrices containing the system coefficients (purely geometrical), $\boldsymbol{U}$ and $\boldsymbol{T}$ are vectors containing the nodes values of velocity and tension, respectively, and $\boldsymbol{B}$ is an independent vector associated to the stress jump on the interface. The linear system can be expressed as

$$\sum_{n=1}^{N_o+N_i}\boldsymbol{H}_{mn}(t)\cdot\boldsymbol{u}_{(n)}(t) = \sum_{n=1}^{N_o+N_i}\boldsymbol{G}_{mn}\cdot\boldsymbol{t}_{(n)}(t) + \sum_{n=1}^{N_o+N_i}\boldsymbol{B}_{mn}(t). \tag{17}$$

Finally, the coefficients $\boldsymbol{H}$, $\boldsymbol{G}$ and $\boldsymbol{B}$ of the linear system are given by:

$$\boldsymbol{H}_{mn}(t) = \begin{cases} c^m\delta_{mn} + \dfrac{1}{4\pi}\displaystyle\int_{\Delta\Gamma_o^n}\boldsymbol{\mathcal{K}}^{mn}\cdot\hat{\boldsymbol{n}}^n(\xi,t)\cdot\boldsymbol{N}(\xi)\,d\Gamma, \;\; n\in[1,N_o];\\ \\ c^m(\lambda+1)\delta_{mn} + \dfrac{1-\lambda}{4\pi}\left(\dfrac{a}{H}\right)\displaystyle\int_{\Delta\Gamma_i^n}\boldsymbol{\mathcal{K}}^{mn}\cdot\hat{\boldsymbol{n}}^n(\xi,t)\cdot\boldsymbol{N}(\xi)\,d\Gamma,\\ n\in[N_o+1,N_o+N_i]; \end{cases} \tag{18}$$

$$\boldsymbol{G}_{mn} = \begin{cases} \dfrac{1}{4\pi}\displaystyle\int_{\Delta\Gamma_o^n}\boldsymbol{\mathcal{J}}^{mn}\cdot\boldsymbol{N}(\xi)\,d\Gamma, \;\; n\in[1,N_o];\\ \\ \boldsymbol{0}, \;\; n\in[N_o+1,N_i+N_o]; \end{cases} \tag{19}$$

and

$$\boldsymbol{B}_{mn}(t) = \begin{cases} \boldsymbol{0}, \;\; n\in[1,N_o];\\ \\ \dfrac{1}{4\pi}Ca^{-1}\displaystyle\int_{\Delta\Gamma_i^n}\boldsymbol{\mathcal{J}}^{mn}\cdot\kappa^n(\xi,t)\hat{\boldsymbol{n}}^n(\xi,t)\,d\Gamma,\\ n\in[N_o+1,N_i+N_o]. \end{cases} \tag{20}$$

To each node should be applied one boundary condition for each direction, velocity or tension. On the channel entrance section is applied the parabolic profile of velocity for a pre-determined mean velocity; On the walls of the channel, there is a no-slip condition, so $\boldsymbol{u}(\boldsymbol{x},t) = \mathbf{0}$; For the channel exit section is defined a pressure equal to zero, so $\boldsymbol{t}(\boldsymbol{x},t) = \mathbf{0}$; Over the fluids interface it is used the Young-Laplace equation, which defines the vector $\boldsymbol{B}$.

Solving the system, it will be obtained the tension and velocity over all nodes. The drop surface is evolved using an Euler first-order equation at each node on the interface, so $\Delta \boldsymbol{x}_0 = \boldsymbol{u}(\boldsymbol{x}_0,t)\,\Delta t$, for a pre-determined time step Δt.

4 RESULTS

This section brings all results obtained in this work, including discussions about it. All results were obtained using a MATLAB® code, considering the same channel geometry, presented in Fig. 2. The channel dimensions are function of the entrance height, H, and it is composed by eight straight segments (1 to 8). The initial drop center is always at the same point, $\boldsymbol{x}_c = (0.4H, 0.5H)$. The drop surface, initially round, is defined by two arcs segments (9 and 10), and the channel convergence ratio is 2:1.

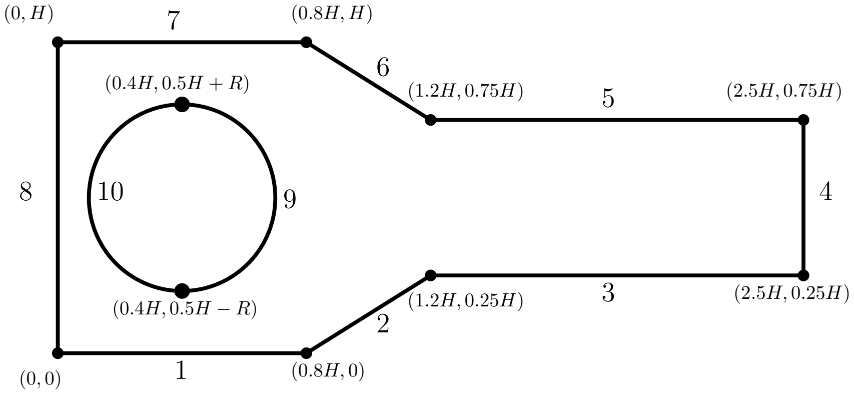

Figure 2: Channel geometry, showing the 10 segments defining the channel and drop contours.

4.1 Mesh convergence

The contour discretization was done using the parameter Ne. Following Fig. 2, the segments 2, 4 and 6 are divided in Ne elements, the segments 1, 7 and 8 are divided in $2Ne$ elements, and the segments 3, 5, 9 and 10 are divided in $3Ne$ elements. The method accuracy, in relation to Ne, was studied for: the absolute error for the outlet flow rate, $|Q_{out}(t) - Q_{in}|/Q_{in}$, being Q_{in} the flow rate imposed at the channel entrance; the drop area error, $|A(t) - A_0|/A_0$, being A_0 the initial drop area; and the convergence for the pump pressure curve to keep the flow rate constant. This study used the parameters: $Ca = 0.25$, $\lambda = 10$, $a = 0.55$ and $\Delta t = 0.01$. All results are presented in Figs. 3 to 5. The parameter x* is given by the coordinate x_1 of the extreme right node of the drop (x_1^r) divided by the channel length, x*= $x_1^r/2.5H$.

The plot in Fig. 3 shows that the absolute error associated to the outlet flow rate decreases considerably with the mesh refinement, and it stays more stable over x*. For $Ne = 3$, this error is around 7.0%, decreasing to 1.0% for $Ne = 9$. Analyzing Fig. 4, the error associated to the area is basically invariant to mesh refinement. The drop area error is associated to the

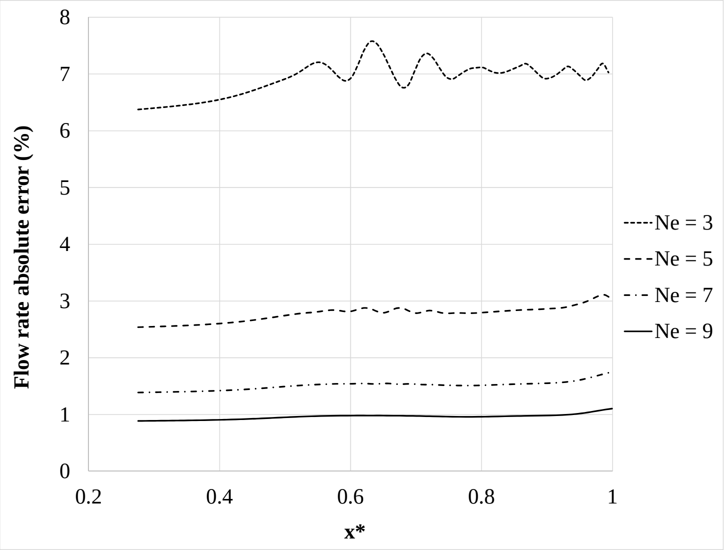

Figure 3: Absolute error obtained for the outlet flow rate in function of Ne.

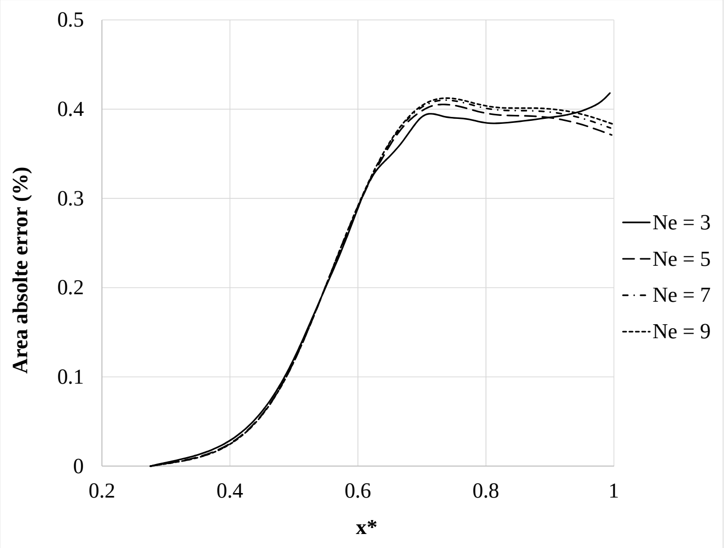

Figure 4: Absolute error obtained for the drop area in function of Ne.

instantaneous shape, which depends essentially to the time step, justifying this fact. But, all errors are low and hit the maximum value around 0.4% at the relative position of x*$= 0.7$ (after the drop enters the throat). Finally, the pressure curves in Fig. 5 show that the pressure depends on the mesh discretization, and they collapse for Ne bigger than 7.

After all these analysis, and considering the balance between accuracy and computational time, $Ne = 7$ was chosen for the other simulations in this work.

4.2 Method stability related to the time step

The time step, Δt, study was done using the following parameters: $Ca = 0.25$, $\lambda = 10$, $a = 0.55$ and $Ne = 7$. The results are shown in Figs. 6 to 8.

Figure 6 shows that the flow rate error is unresponsive to the temporal refinement employed

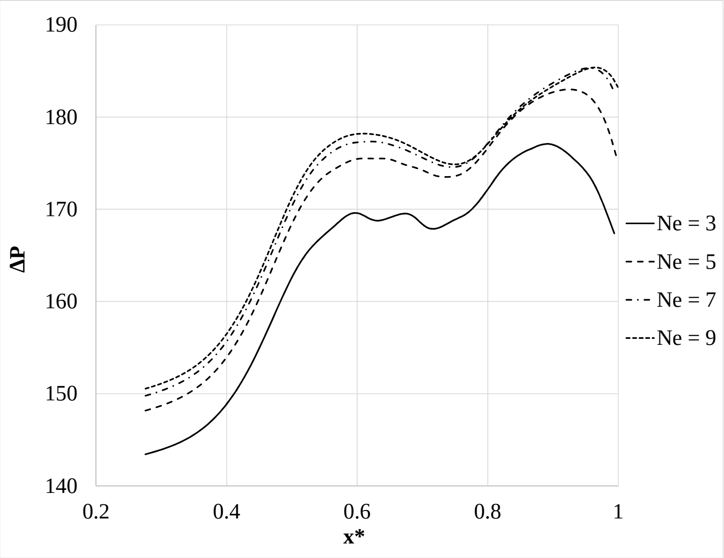

Figure 5: Pump pressure curve obtained in function of Ne.

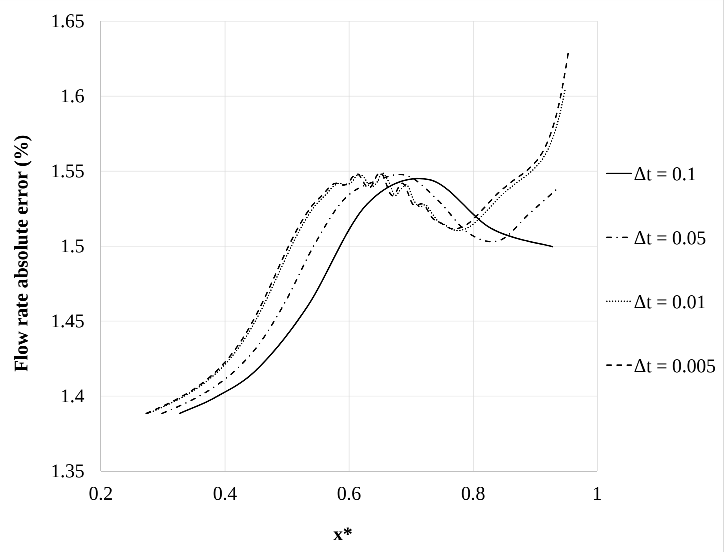

Figure 6: Absolute error obtained for the outlet flow rate in function of Δt.

to the Euler method. In fact this error only depends on the mesh discretization. Anyway, the numeric error remained low and between 1.4% and 1.6%. The curves tend to collapse when the Δt is reduced. In contrast, the area error is affected a lot by the time step refinement, as it is shown in Fig. 7. For $\Delta t = 0.1$ the maximum error is around 4.75%, reducing to 0.25% for $\Delta t = 0.005$. Finally, the pressure curve tends to collapse when Δt is decreased. In fact, the curves for $\Delta t = 0.01$ and $\Delta t = 0.005$ are considerably close, as shown in Fig. 8. Due these analysis, it was chosen $\Delta t = 0.01$ for the next simulations.

4.3 Capillary number effect

Capillary number is one the main parameters in the study of mechanics and rheology of emulsions, being defined as the viscous and inertial forces ratio, originated by the interfacial

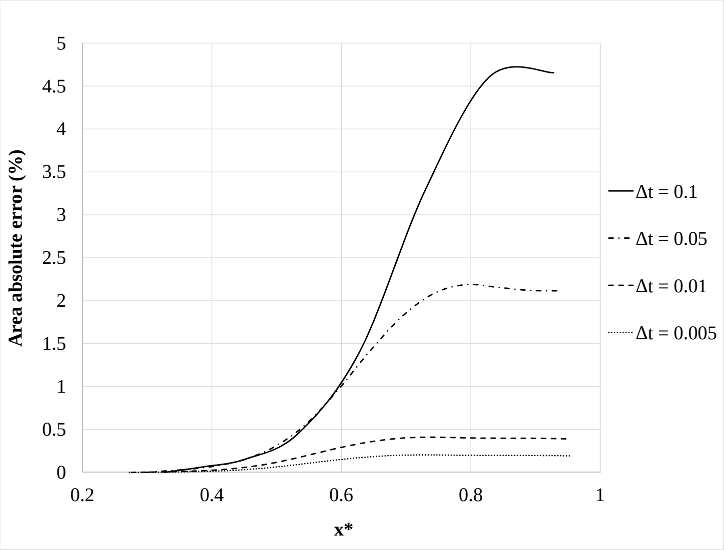

Figure 7: Absolute error obtained for the drop area in function of Δt.

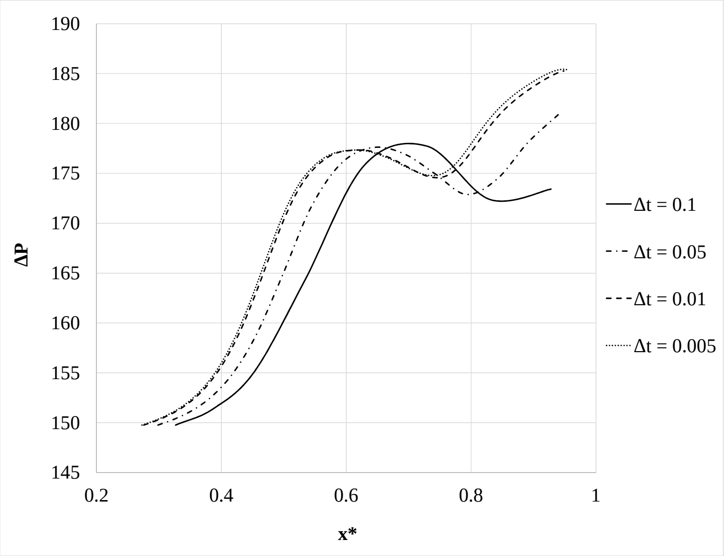

Figure 8: Pump pressure curve obtained in function of Δt.

tension between two fluids. Here, it is defined as $Ca = \mu U/\sigma$. The interfacial tension acts to maintain the drop with a round geometry. The channel geometry forces the drop to deform due to the flow extensional character. In other hand, the capillary forces try to restore your spherical original geometry. As a result, the flow increase the pump pressure, forcing the drop to enter the convergence and keep a constant flow rate. This pump pressure increase can recover trapped oil in neighboring ganglia. Figures 9 and 10 show moments of the drop through the channel for: $Ca = 1.0$ and $Ca = 0.0625$; $\lambda = 30$ and $a = 0.55$.

Analyzing Figs. 9 and 10, smaller Ca values results in rounder drops, smoother shapes. The Young-Laplace equation shows that bigger σ and bigger curvatures cause higher tensions, pushing the drop surface to its curvature center, tending to keep the drop rounder.

Figure 11 brings moments of the drop for $Ca = 0.0625$, $\lambda = 10$ and $a = 0.55$, and

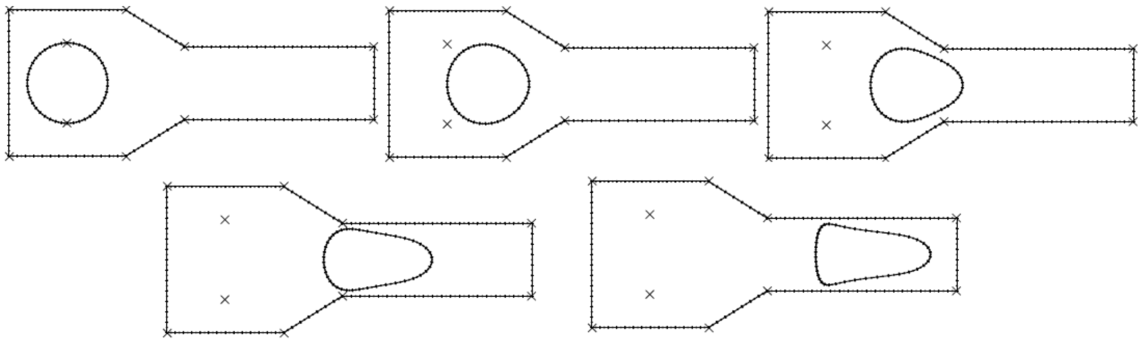

Figure 9: Moments of the drop flowing through the channel, for $Ca = 1$.

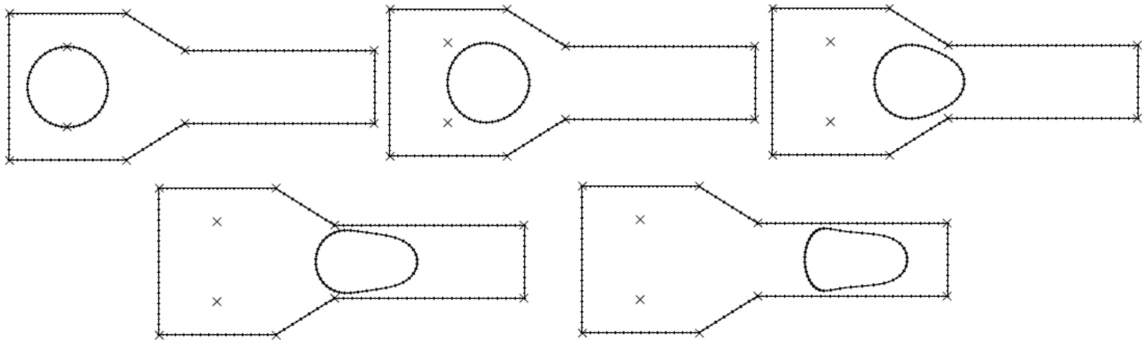

Figure 10: Moments of the drop flowing through the channel, for $Ca = 0.0625$.

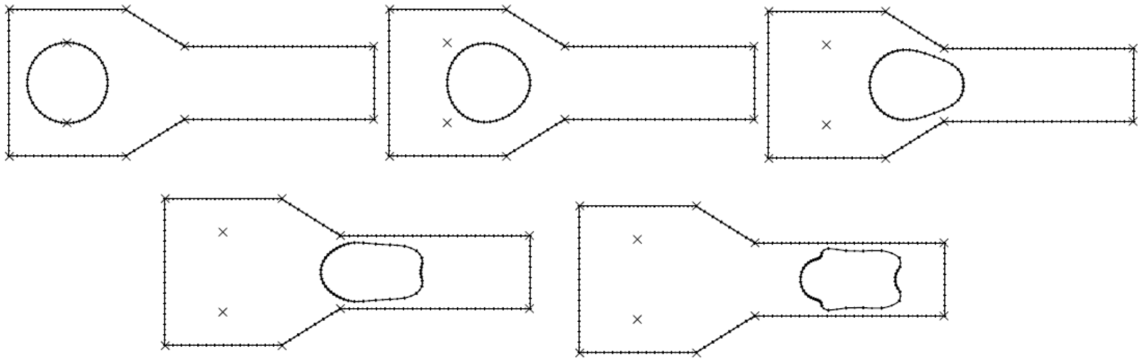

Figure 11: Moment of the drop through the channel, for $Ca = 0.0625$, $\lambda = 10$ and $a = 0.55$.

shows that the drop assumed an unexpected geometry, indicating a method instability in one or more instants of the simulation. This instability can happen for three reasons (or a combination of them): A high curvature somewhere on the drop surface created a high tension, resulting in a fast evolution for which the time-step was not refined enough to capture the deformation smoothly. Discontinuities on the surface, as it is shown in Fig. 12, results in wrong curvature calculations. Curvatures centered outside the drop were not expected in the formulation, being one of the instabilities causes. The first and the second mentioned causes can be corrected refining even more the time-step and the mesh, respectively. The third cause requires a method to recognize concave and convex surfaces. There are, in the literature, some techniques to control the simulations avoiding instabilities. Yan et al. (2006) calculated the time-step in each iteration using a maximum node displacement allowed. Another authors prefer to calculate the time-step in function of the drop relaxation characteristic time (Oliveira, 2007). It was not found in the literature a method to treat the discontinuities over the drop surface for continuous quadratic elements.

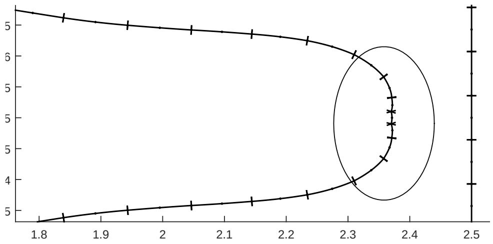

Figure 12: Drop surface discontinuities after a high deformation, for $Ca = 0.25$ and $\lambda = 10$.

With the drop deformation, the nodes over the surface are no longer equally distributed, they tend to be concentrated in the front and back part of the drop. This fact does not seem to be a problem for the method stability and accuracy, because these two regions present the surface higher curvatures, in other words, they need more careful treatment in the method. However, Wrobel et al. (2009) showed a node relocation method, used in each iteration, to keep the nodes equally spaced during the simulation.

Figure 13 shows the capillary number influence over the pump pressure[2] curve. Smaller capillary number represents higher pump pressure. It can be noticed that the greater pressure increase happens between x*$= 0.4$ and x*$= 0.6$, when the drop is passing through the convergence (higher deformations). After the drop enters in the channel, the pump pressure oscillates around the value reached in the constriction region.

The relative point x*$= 0.59$ was adopted as reference to do a deeper analysis on capillary number influence over the pressure behavior. For different viscosity ratio values, this relation is shown in Fig. 14. This plot basically shows a linear relation between Ca^{-1} and $\Delta P/P^*$.

4.4 Viscosity ratio effects

The subject, now, will be the study of viscosity ratio, λ, effects over the drop flow through the converging channel. Figure 15 shows the shape of 5 different drops at the same moment. For all cases $Ca = 0.25$ and $a = 0.55$, but the viscosity ratios are different.

---

[2] P^* is the pressure difference obtained for the flow in the channel without the drop presence, where $P^* = 149$.

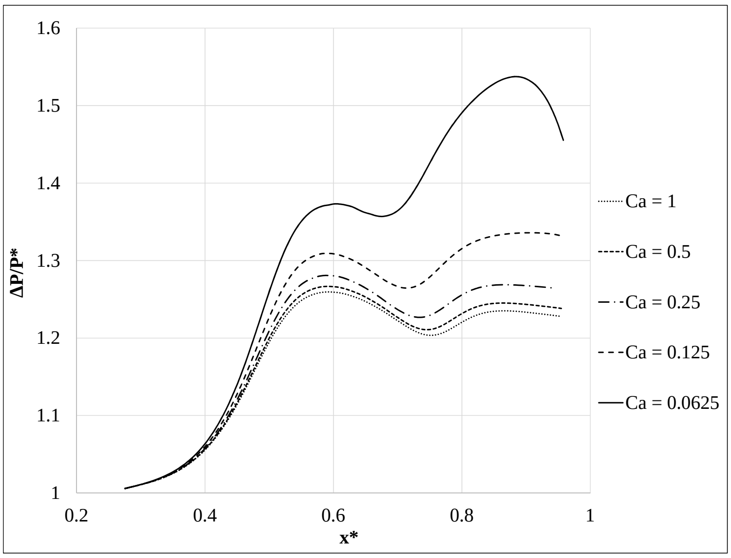

Figure 13: Pump pressure curves obtained in function of Ca, for $\lambda = 20$.

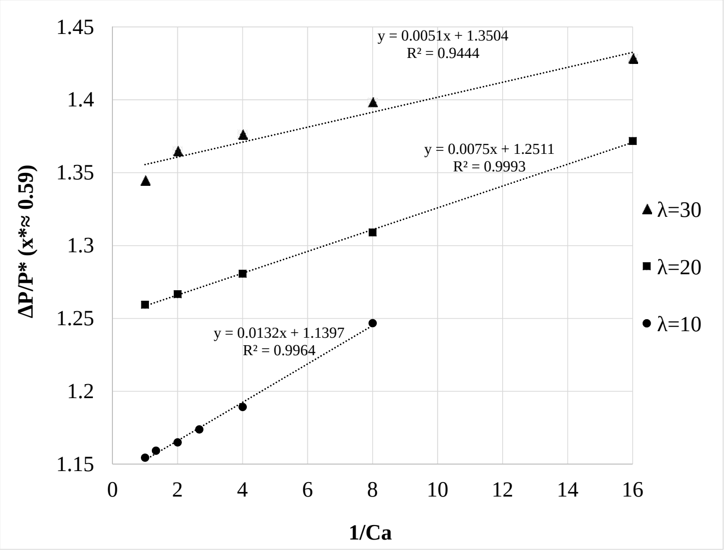

Figure 14: Pump pressure for x*$= 0.59$ in function of Ca^{-1} for different λ values.

From Fig. 15, higher viscosity ratios reduce the drop deformation. In fact, the higher is the viscosity ratio, the higher is the droplet deformation resistance. Note that, while capillary forces tend to make the drop round, the viscosity ratios act on your deformation resistance.

The Fig. 16 clearly shows the influence of viscosity ratio over $\Delta P/P^*$ curves. Higher values for λ imply higher values for pump pressure. All curves present a similar shape. Figure 17 presents the obtained values to $\Delta P/P^*$ for the relative drop position x*$= 0.59$ for different λ. This plot shows that the relation between $\Delta P/P^*$ and λ is basically linear and positive.

4.5 Initial drop diameter effects

Finally, the initial drop diameter, a, effects in the flow was studied. Figures 18 to 20 show the drop form for different sizes through the channel. For all cases, $\lambda = 10$ and $Ca =$

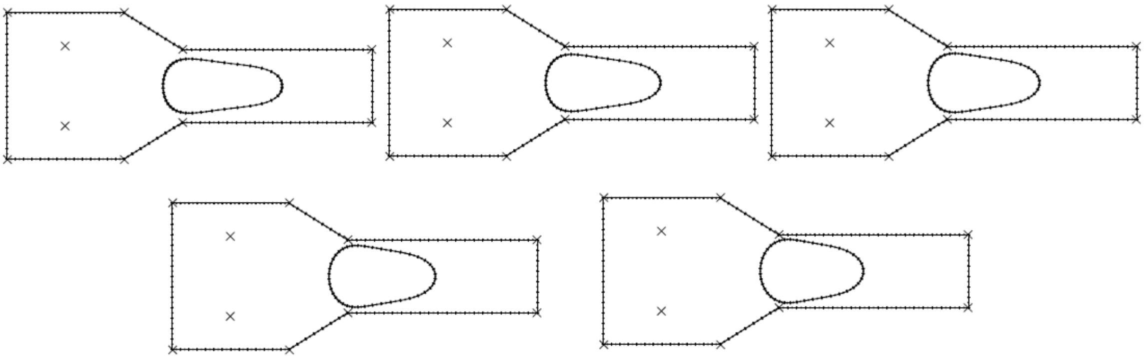

Figure 15: Drop shapes for the same instant. From the left to the right, $\lambda = 10, 15, 20, 30$ and 40, respectively.

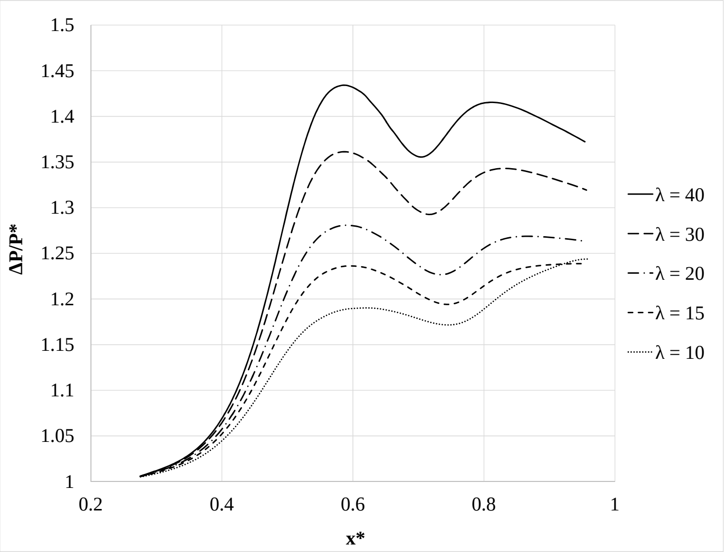

Figure 16: Pump pressure in function of λ, for $Ca = 0.25$.

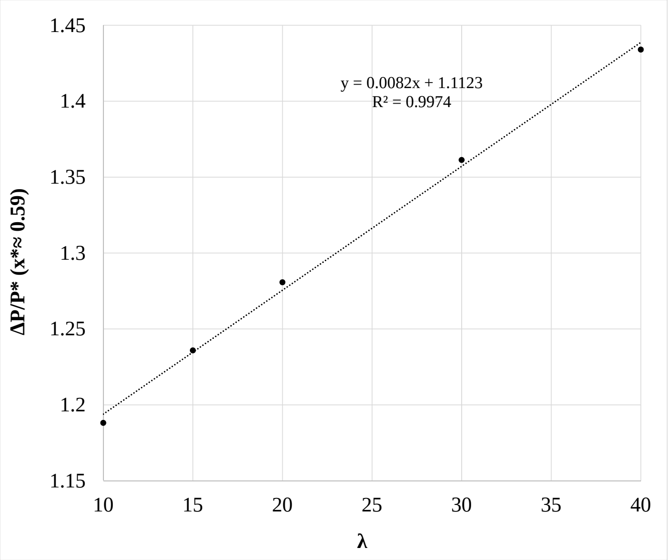

Figure 17: Pump pressure for x*$= 0.59$ in function of λ, for $Ca = 0.25$.

0.25. Bigger drops need to deform more to pass through the channel throat, confirming the high extensional flow character close to the constriction. Consequently, the pump pressure is increased, as it is shown in Fig. 21. Figure 22 brings the maximum pressure obtained in the flow in function of the drop initial diameter.

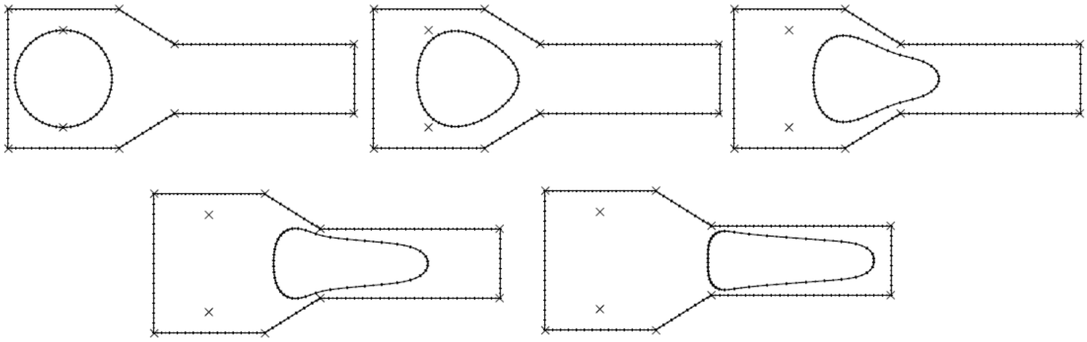

Figure 18: Drop shapes through the channel, for $a = 0.70$.

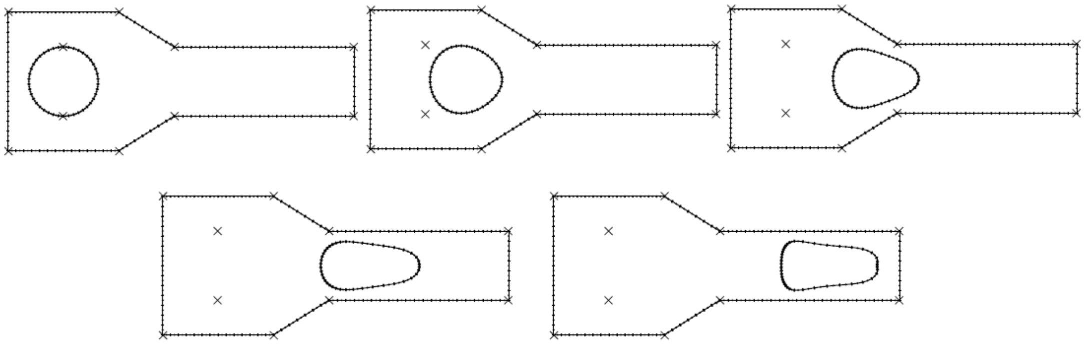

Figure 19: Drop shapes through the channel, for $a = 0.50$.

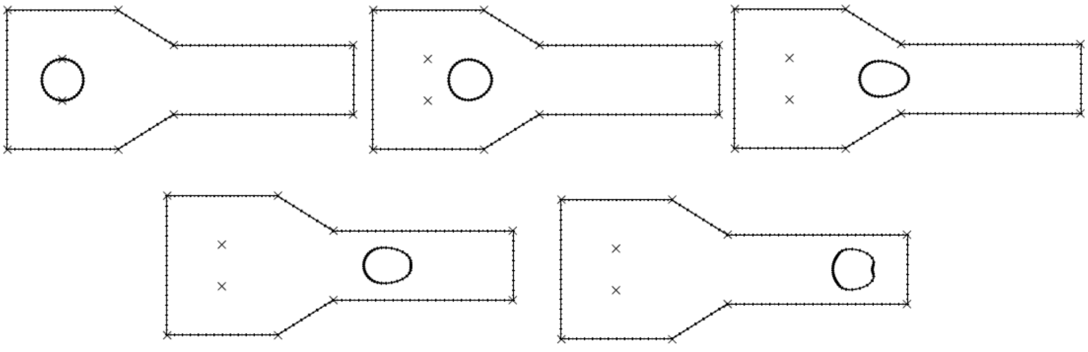

Figure 20: Drop shapes through the channel, for $a = 0.30$.

Figure 21 confirms the increase for the pump pressure as bigger the drop initial diameter is. This phenomenon is consequence of the higher drop strain rate when it is crossing the constriction, increased with the drop diameter. In Fig. 20, the last moment exposed for this drop size showed an instability, which did not happen to the others two cases. Smaller radii are associated to intense curvatures, and how it was said before, curvature is the parameter which creates more problems for the method. Finally, Fig. 22 shows a relation, approximately quadratic, between the maximum $\Delta P/P^*$ and a.

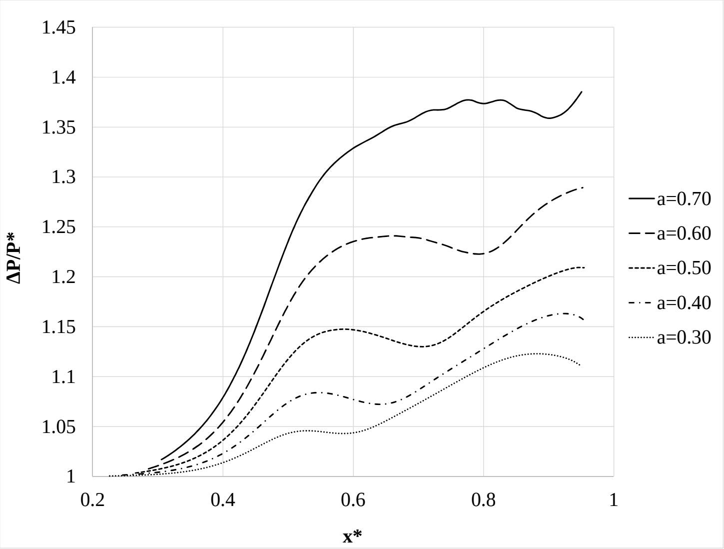

Figure 21: Pump pressure in function of the drop initial diameter a, for $Ca = 0.25$ and $\lambda = 10$.

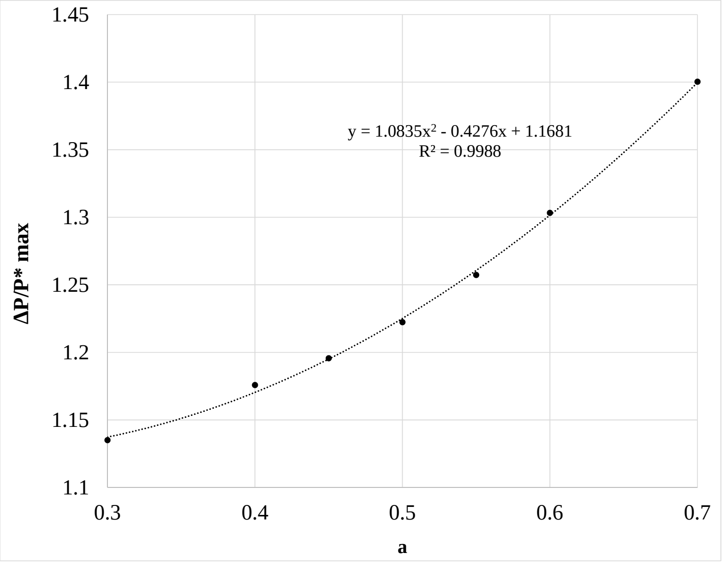

Figure 22: Maximum pump pressure in function of a, for $Ca = 0.25$ and $\lambda = 10$.

5 CONCLUSIONS

The Boundary Element Method was used to study the effect of physical and geometrical parameters on the flow of an emulsion drop through a converging channel. First, the convergence and accuracy of the method were studied in relation to the mesh and time step refinement. The two parameters used for that error study were the numerical error for the outlet flow rate and drop area, both considering the mass conservation and the fluids incompressibility. By these results, the parameter for the number of elements chose was $Ne = 7$, which presents an error around 1.5% for the outlet flow rate, and a time step $\Delta t = 0.01$, presenting smaller errors than 0.5% for the drop area. After the determination of these two simulation parameters, the study of the capillary number (Ca), viscosity ratio (λ) and drop initial diameter (a) effects were carried out. In relation to the drop shapes, smaller Ca makes the drop rounder, while bigger λ makes the drop more resistant to deformations. As bigger it is a, more deformation is suffered by the drop to enter the constriction. The pump pressure increases for smaller Ca, bigger λ and bigger a. The relation between Ca^{-1} and $\Delta P/P^{*}$ is basically linear and positive. The same happens between λ and $\Delta P/P^{*}$. While, between a and $\Delta P/P^{*}$ is still positive, but quadratic.

REFERENCES

Alvarado, V. & Manrique, E., 2010. *Enhanced Oil Recovery: Field Planning and Development Strategies*. Elsevier, 1 ed.

Kim, S. & Karrila, S. J., 1991. *Microhydrodynamics - Principles and Selected Applications*. Butterworth-Heinemann.

Khayat, R. E., Luciani, A. & Utracki, L.A., 1997. Boundary-element analysis of planar drop deformation in confined flow. *Engineering Analysis with Boundary Elements*, vol. 19, pp. 279-289.

Ladyzheskaya, O. A., 1969. *The Mathematical Theory of Viscous Incompressible Flow*. Gordon & Breach.

Oliveira, T. F., 2007. *Microhidrodinâmica e Reologia de Emulsões*. Doctorate Degree Thesis - PUC-Rio, RJ, Brazil.

Pozrikidis, C., 1992. *Boundary Integral and Singularity Methods for Linearized Viscous Flow*. Cambridge University Press.

Roca, J. F. & Carvalho, M. S., 2013. Flow of a drop through a constricted microcapillary. *Computer & Fluids*, vol. 87, pp. 50-56.

Wrobel, L. C., Júnior, D. S., & Bhaumik, C. L., 2009. Drop deformation in Stokes flow through converging channels. *Engineering Analysis with Boundary Elements*, vol. 33, pp. 832-844.

Yan, L., Thompson, K. E., & Valsaraj, K. T., 2006. A numerical study on the coalescence of emulsion droplets in a constricted capillary tube. *Journal of Colloid and Interface Science*, vol. 298, pp. 832-844.